



Tricuspid Chordae Tendineae Mechanics: Insertion Site, Leaflet, and Size-Specific Analysis and Constitutive Modelling

K. J. Smith¹ · M. Mathur² · W. D. Meador³ · B. Phillips-Garcia⁴ · G. P. Sugerman³ · A. K. Menta³ · T. Jazwiec^{5,6} · M. Malinowski^{5,7} · T. A. Timek⁵ · M. K. Rausch^{1,3,8}

Received: 30 December 2019 / Accepted: 20 April 2020 / Published online: 8 June 2020
© Society for Experimental Mechanics 2020

Abstract

Background: Tricuspid valve chordae tendineae play a vital role in our cardiovascular system. They function as “parachute cords” to the tricuspid leaflets to prevent prolapse during systole. However, in contrast to the tricuspid annulus and leaflets, the tricuspid chordae tendineae have received little attention. Few previous studies have described their mechanics and their structure-function relationship. **Objective:** In this study, we aimed to quantify the mechanics of tricuspid chordae tendineae based on their leaflet of origin, insertion site, and size. **Methods:** Specifically, we uniaxially stretched 53 tricuspid chordae tendineae from sheep and recorded their stress-strain behavior. We also analyzed the microstructure of the tricuspid chordae tendineae based on two-photon microscopy and histology. Finally, we compared eight different hyperelastic constitutive models and their ability to fit our data. **Results:** We found that tricuspid chordae tendineae are highly organized collagenous tissues, which are populated with cells throughout their thickness. In uniaxial stretching, this microstructure causes the classic J-shaped nonlinear stress-strain response known from other collagenous tissues. We found differences in stiffness between tricuspid chordae tendineae from the anterior, posterior, or septal leaflets only at small strains. Similarly, we found significant differences based on their insertion site or size also only at small strains. Of the models we fit to our data, we recommend the Ogden two-parameter model. This model fit the data excellently and required a minimal number of parameters. For future use, we identified and reported the Ogden material parameters for an average data set. **Conclusion:** The data presented in this study help to explain the mechanics and structure-function relationship of tricuspid chordae tendineae and provide a model recommendation (with parameters) for use in computational simulations of the tricuspid valve.

Keywords Ogden · Fung · Mooney-Rivlin · Two-Photon microscopy · Histology · Structure-function relationship · Uniaxial tensile testing

Introduction

The tricuspid valve controls flow through the right atrioventricular orifice of the heart. During the cardiac cycle, the three leaflets of the valve open to direct anterograde blood flow from the right atrium into the right ventricle and close to prevent retrograde blood flow from the right ventricle into the right atrium. In the closed position, the three leaflet edges coapt and seal the

atrioventricular orifice. As the right ventricle pressurizes, tricuspid chordae tendineae, which attach the leaflets to the papillary muscles and ventricular wall, prevent the valve from prolapsing. Thus, tricuspid chordae tendineae function like “parachute cords”, suspending the pressurized leaflets [1, 2]. Additionally, tricuspid chordae tendineae may provide structural stability to the ventricular myocardium. For the mitral valve, it has been shown that chordal sparing during mitral valve replacement is paramount to preventing subsequent left ventricular dilation. Tricuspid chordae tendineae may fulfill a similar role on the right side of the heart [3].

Historically, the tricuspid valve received little attention in comparison to its left-side equivalent, the mitral valve [4, 5]. However, recent acknowledgment of the valve’s

✉ M. K. Rausch
manuel.rausch@utexas.edu



role in cardiovascular disease has sparked new enthusiasm for studying the valve and its mechanics [6]. Mechanical studies have specifically focused on predictive computer models to study the normal valve and the influence of surgical intervention or transcatheter therapies [7–10]. Naturally, increased modeling efforts have increased the demand for accurate material data. However, information on the mechanics of the tricuspid chordae tendineae, while critically important, is sparse. The first reports of the mechanical properties of tricuspid chordae tendineae came from studies performed by Lim et al. [11, 12]. These studies tested specimens from healthy patients of moderate age and patients with myxomatous valves. More recently, an extensive study on the mechanics of porcine tricuspid leaflets (including their chordae tendineae) was performed by Pokutta-Paskaleva et al. [13].

In our current study, we provide a detailed mechanical analysis of the tricuspid chordae tendineae of sheep, which are a widely accepted large animal model for cardiac disease research [14]. Specifically, our goal is to report the insertion-site-, leaflet-, and size-specific material properties of tricuspid chordae tendineae via uniaxial tensile testing and to supplement these data via quantitative two-photon-based analyses of collagen orientation and cell nuclei distribution and shape, as well as histology. Finally, we compare eight different material models to describe these data.

Methods

We performed all experimental and animal procedures in congruence with the Guide for Care and Use of Laboratory Animals prepared by the National Academy of Science and published by the National Institutes of Health, and the Principles of Laboratory Animal Care, formulated by the National Society for Medical Research. The study protocol was approved by our local Institutional Animal Care and Use Committee (Spectrum Health IACUC No.: 18-01).

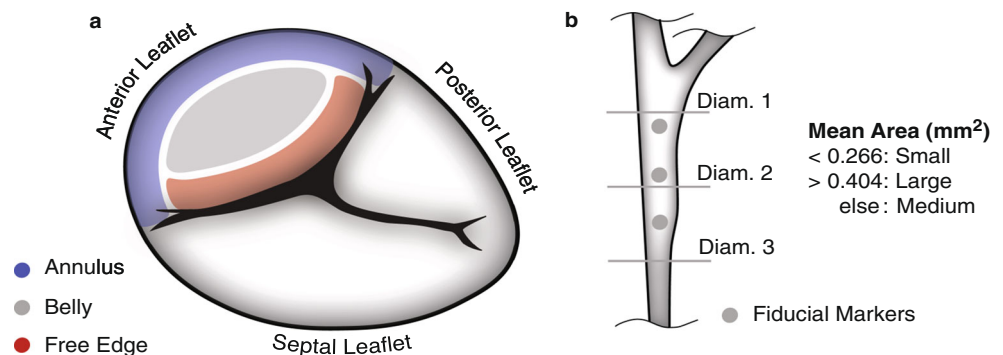
Animal Procedures and Sample Preparation

After sacrificing nine male Dorset Sheep, we excised their tricuspid valves, isolated individual leaflets from the tricuspid valve and cryogenically stored them at $-80\text{ }^{\circ}\text{C}$ in a 9:1 DMEM and DMSO solution with a protease inhibitor [15]. Before use, we rapidly thawed the tissue and excised the tricuspid chordae tendineae, separating each into a single strut, noting their insertion site. After excising the tricuspid chordae tendineae, we measured the chordal diameter of each sample at three locations using a 4x objective on a light microscope (*BX53 Upright Microscope, Olympus, Tokyo, Japan*), see Fig. 1b, and averaged the three diameters. We then classified the tricuspid chordae tendineae by leaflet as Anterior, Posterior or Septal, and by insertion site as Free Edge, Belly, and Annulus as seen in Fig. 1a. Furthermore, we classified them as small (area $< 0.266\text{ mm}^2$), large (area $> 0.404\text{ mm}^2$), and medium (else) as shown in Fig. 1b. We chose the cut-off for the small, medium, and large tricuspid chordae tendineae so as to create approximately equal-sized groups. Upon classification, tissues were allocated to one of three experiments: Mechanical Testing, Two-Photon Imaging, or Histology.

Mechanical Testing

On tricuspid chordae tendineae allocated for mechanical testing, we marked three fiducial markers along the central shaft with ink dots (spaced approximately 2 mm apart). Using a custom clamp system, we mounted the sample on a commercial uniaxial mechanical testing device (*Univert, Cellscale, Waterloo, Ontario, Canada*). Applying the previously acquired average diameter and assuming a circular cross-sectional area, we then calculated the tensile force necessary to achieve 1 MPa 1st Piola-Kirchhoff (PK) stress for each sample. Next, we preconditioned the sample to 1 MPa for 10 cycles. On the final loading stroke, we recorded (5 Hz) axial force, clamp-to-clamp distance, and

Fig. 1 **a** Tricuspid chordae tendineae insertion-site and leaflet nomenclature. **b** Chordae tendineae size nomenclature. Also shown are the fiduciary markers used for strain calculations



images of the fiducial markers to compute local tissue stretch via digital image correlation. We conducted all tests using a 1.5 N load cell in a 37 °C bath of 1xPBS within 4 h of thawing.

Two-Photon Imaging and Histology

To prepare tricuspid chordae tendineae for two-photon imaging, we first counterstained the tissue for cell nuclei (*Hoechst 33342*, Thermo Fischer Scientific, Waltham, MA, USA) in staining buffer for 20 min. Prior to imaging, we also optically cleared the tissue using an isotonic glycerol optical clearing solution (50:30:20% Glycerol, DMSO and 5xPBS, respectively). We then transferred the samples to a two-photon microscope (*Ultima IV*, Bruker, Billerica, MA, USA) and placed them on foil-lined microscope slides which functioned as visual indicators of full-thickness image acquisition. Utilizing second harmonic generation (SHG) to view collagen fibers and fluorescence to view cell nuclei, we used excitation wavelengths of 900 nm and 800 nm, respectively, and epi-collected the back-scattered signal with a PMT channel filter (460 nm \pm 25 nm). With a 20 \times water immersion objective (*XLUMPLFN*, Olympus, Center Valley, PA, USA), we acquired z-stack images (10 μ m steps) from the tissue's top surface to the underlying foil in two 500 \times 500 μ m locations along the tissue shaft. During imaging, the samples were beneath a coverslip in a stress-free configuration (i.e., no external tension applied). To analyze the collagen fibers and nuclei we implemented a previously introduced method of morphological quantification [15, 16]. In short, we first normalized each collagen image histogram based on saturation. In this study, due to collagen undulation appearing in and out of plane, we applied a high-pass Fourier transform filter to reduce periodic "banding". We passed these filtered images into the *ImageJ* plugin *OrientationJ* [17], providing a coherency-weighted histogram of fiber orientations for each image. With histogram interpolation, we averaged across both locations of a single sample to acquire a single z-stack of histograms by depth for each sample, where 0% and 100% depths represent the top and bottom surfaces, respectively. We then fit a von Mises distribution to these histograms and averaged the parameters μ and κ , i.e., the mean fiber angle and the fiber orientation concentration, respectively, across all samples at each depth. To analyze nuclei images, we passed the images into a custom *MATLAB* program, which identifies each individual nucleus and calculates metrics of orientation, circularity, and nuclear aspect ratio (NAR). We performed similar histogram interpolation as with the SHG images to allow for averaging across locations, to which we then fit von Mises distributions (nuclear orientation) or

normal distributions (circularity and NAR), with parameters μ and σ (i.e. mean and standard deviation, respectively).

Tricuspid chordae tendineae analyzed via histology were fixed in 10% neutral-buffered formalin for 24 h before desiccation in ethanol. Subsequently, we briefly processed the tissue in xylene and embedded in paraffin. We sliced the tissue to 5 μ m thickness and mounted it on slides, which were then stained with either hematoxylin and eosin (H&E) or Picosirius red using standard protocols. We then imaged transverse sections with a light microscope (*BX53 Upright Microscope*, Olympus, Tokyo, Japan) and a 10 \times objective.

Constitutive Models

We fit eight hyperelastic constitutive models, defined by the scalar-valued strain energy function $W(\lambda_1, \lambda_2, \lambda_3)$, to stress-strain data from our uniaxial tensile tests. To this end, we used a least-squares regression algorithm to minimize the error between the measured stress and the stress computed based on each constitutive model, with

$$\sigma_i = \lambda_i W_i + p, \quad (1)$$

where λ_i is the stretch in the i 'th principal direction and W_i are the partial derivatives of the strain energy with respect to the principle stretches, i.e., $W_i = \partial W / \partial \lambda_i$. The scalar penalty parameter p was used to enforce incompressibility. We solved for p under the assumption of stress-free lateral boundary conditions, $\sigma_2 = \sigma_3 = 0$, viz.,

$$p = -\lambda_2 W_2. \quad (2)$$

Under the additional assumption of tissue incompressibility, i.e., $\lambda_1 \lambda_2 \lambda_3 = 1$, with $\lambda_1 = \lambda$ and $\sigma_1 = \sigma$, Eq. 1 simplifies to,

$$\sigma = \lambda W_1 - \lambda^{-1/2} W_2. \quad (3)$$

The results of our uniaxial tensile test data are presented below as 1st PK stress, which we obtained from Eq. 3 through the transformation $P = \lambda^{-1} \sigma$. For detailed derivations see [18].

The strain energy functions used and their derivatives with respect to principal stretches are listed in Table 1. Strain energy functions are expressed through the first and second invariants of the right Cauchy-Green stretch tensor, $I_1 = \lambda^2 + 2\lambda^{-1}$ and $I_2 = 2\lambda + \lambda^{-2}$, respectively.

Statistics

We examined differences in stiffness of the tricuspid chordae tendineae based on leaflet, insertion site, and diameter using a linear mixed-effects model as implemented



Table 1 Hyperelastic strain energy functions (without penalty term for volumetric deformation) and their derivatives with respect to principal stretches

Model	Strain Energy and Derivatives		
Neo-Hooke (Model 1)	W	=	$C_1[I_1 - 3]$
	W_1	=	$2C_1\lambda$
	W_2	=	$2C_1\lambda^{-1/2}$
Fung (Model 2)	W	=	$C_1[\exp(C_2[I_1 - 3]) - 1]/C_2$
	W_1	=	$2C_1\lambda \exp(C_2\beta)$
	W_2	=	$2C_1\lambda^{-1/2} \exp(C_2\beta)$,
where	β	=	$\lambda^2 + 2\lambda^{-1} - 3$
Mooney-Rivlin (Model 3)	W	=	$C_1[I_1 - 3] + C_2[I_2 - 3]$
	W_1	=	$2C_1\lambda + 4C_2$
	W_2	=	$2C_1\lambda^{-1/2} + 2C_2[\lambda^{3/2} + \lambda^{-3/2}]$
Yeoh-2 (Model 4)	W	=	$\sum_{i=1}^2 C_i [I_1 - 3]^i$
	W_1	=	$\sum_{i=1}^2 2i C_i \lambda \beta^{i-1}$
	W_2	=	$\sum_{i=1}^2 2i C_i \lambda^{-1/2} \beta^{i-1}$
where	β	=	$\lambda^2 + 2\lambda^{-1} - 3$
Ogden-2 (Model 5)	W	=	$C_1[\lambda^{C_2} + 2\lambda^{-C_2} + \lambda^{-C_2} - 3]/C_2$
	W_1	=	$C_1\lambda^{C_2-1}$
	W_2	=	$C_1\lambda^{-(C_2-1)/2}$
Neo-Fung (Model 6)	W	=	$C_1[I_1 - 3] +$
		+	$C_2[\exp[C_3(I_1 - 3)] - 1]/2C_3$
	W_1	=	$2C_1\lambda + 2C_2\lambda \exp(C_3\beta)$
	W_2	=	$2C_1\lambda^{-1/2} + 2C_2\lambda^{-1/2} \exp(C_3\beta)$
where	β	=	$\lambda^2 + 2\lambda^{-1} - 3$
Yeoh-3 (Model 7)	W	=	$\sum_{i=1}^3 C_i [I_1 - 3]^i$
	W_1	=	$\sum_{i=1}^3 2i C_i \lambda \beta^{i-1}$
	W_2	=	$\sum_{i=1}^3 2i C_i \lambda^{-1/2} \beta^{i-1}$
where	β	=	$\lambda^2 + 2\lambda^{-1} - 3$
Ogden-4 (Model 8)	W	=	$C_1[\lambda^{C_2} + \lambda_2^{C_2} + \lambda_3^{C_2} - 3]/C_2$
		+	$C_3[\lambda^{C_4} + \lambda_2^{C_4} + \lambda_3^{C_4} - 3]/C_4$
	W_1	=	$C_1\lambda^{C_2-1} + C_3\lambda^{C_4-1}$
	W_2	=	$C_1\lambda^{-(C_2-1)/2} + C_3\lambda^{-(C_4-1)/2}$

in R [19]. In our model insertion site, leaflet, and area were considered as fixed effects and subject as a random effect. Subsequently, we used an ANOVA and Tukey-Kramer multi-comparison analyses to isolate the effects of individual groups. We performed Pearson correlation tests to analyze any linear correlations in our data. P-values smaller than 0.05 were defined to be statistically significant. We report all data as mean values \pm standard error, unless indicated otherwise.

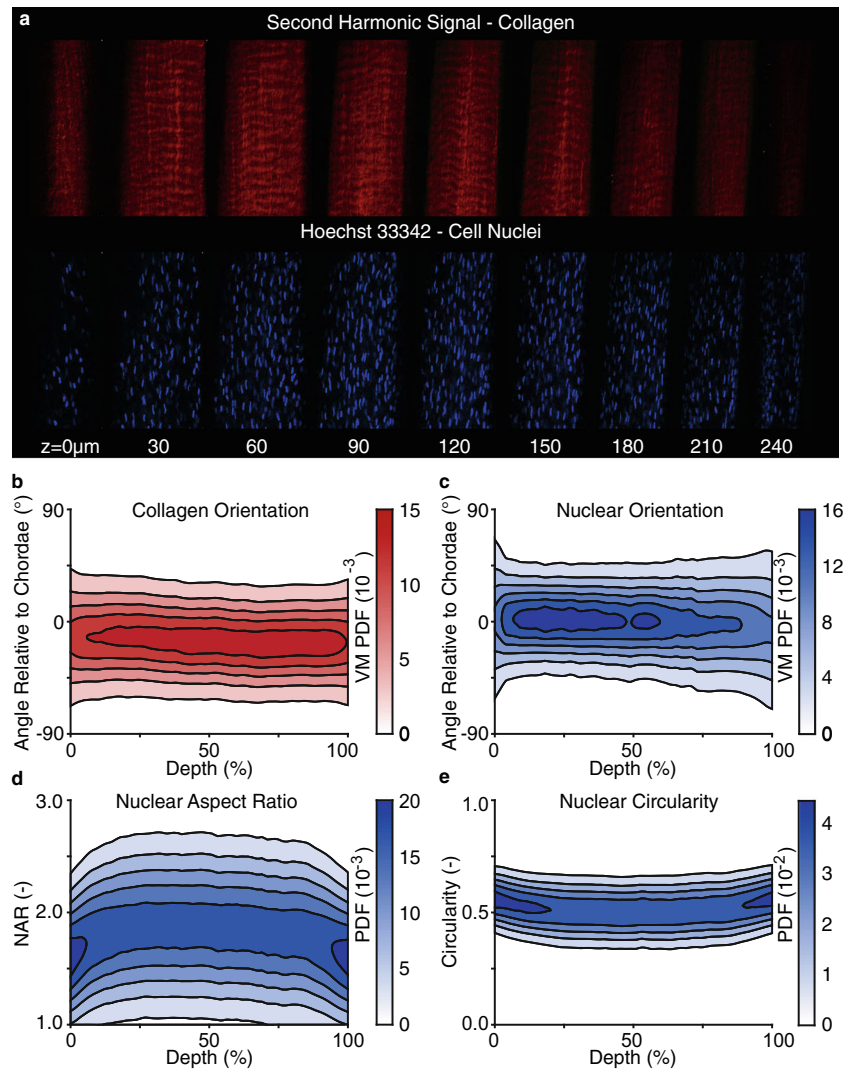
Results

Toward understanding the microstructure of tricuspid chordae tendineae, we successfully captured two-photon microscopy images of collagen and cell nuclei from 14 samples with at least one full-thickness image stack per leaflet and per insertion site. Qualitatively, we observed

no major differences between the collagen and cell nuclei microstructure with respect to leaflet, insertion site, and size, including collagen waviness. We observed that all tricuspid chordae tendineae were highly organized collagenous tissues that, when stress-free, presented with undulated, yet unidirectional, collagen (Fig. 2a). Collagen was present at all depths of the tissues and oriented along the shaft of the tricuspid chordae tendineae. Cell nuclei were also present at all depths of the tissue. Our quantitative analysis of one representative sample confirmed that collagen orientation aligned preferentially in the direction of the chordal shaft (Fig. 2b). Throughout, and especially in areas of dense collagen alignment, cell nuclei presented with an elongated and undulated morphology and paralleled the neighboring collagen (Fig. 2c-e). At the surface of the tissues, cell nuclei were less elongated (i.e., NAR closer to 1) and more circular (i.e., circularity closer to 1), suggestive of the endothelial cell layer. Overall, our



Fig. 2 Tricuspid chordae tendineae have a wavy, but unidirectionally orientated collagen architecture and are populated with cells that are oriented with the collagen. **a** Fluorescent collagen and cell nuclei depiction of representative small tricuspid chordae tendineae from a posterior leaflet and the belly site. Top: Second Harmonic Generation images show a wavy but unidirectionally oriented collagen organization. Bottom: Hoechst 33342-based depiction of cell nuclei that are present throughout the entire tricuspid chordae tendineae thickness and length. **b** von Mises (VM) probability density functions (PDF) of collagen orientation throughout the depth of the tissue (from the top surface to the bottom surface), relative to the tricuspid chordae tendineae longitudinal direction. **c-e** PDFs of cell nuclei metrics. Specifically, **c** orientation relative to tricuspid chordae tendineae direction, **d** nuclear aspect ratio (NAR), and **e** circularity throughout the tissue depth



findings indicate that tricuspid chordae tendineae are highly organized unidirectional collagenous structures with a dense and aligned cell population throughout.

We supported our two-photon based analysis via histology. Specifically, we stained tissue cross-sections of four chordae with H&E and Picrosirius red. H&E highlights the

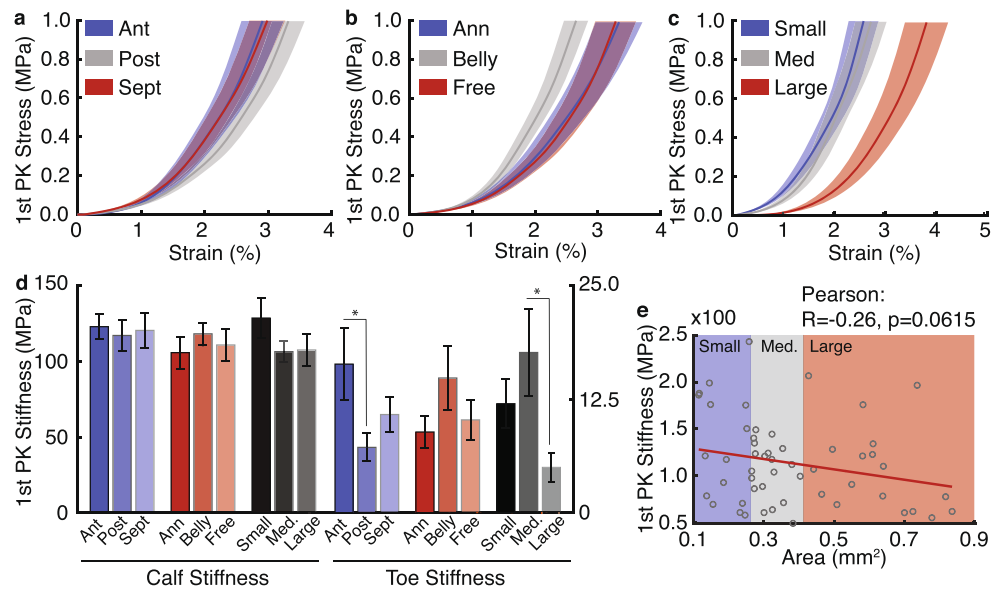
extracellular matrix and cytoplasm pink, while it renders cell nuclei dark purple. Representative images in Fig. 3a-c illustrate the abundance of collagen throughout the tissue thickness and the presence of cell nuclei throughout.

Before analysing our uniaxial tensile test data, we excluded data sets of poor quality. Specifically, we excluded



Fig. 3 Cross-sectional stains of a representative tricuspid chordae tendineae support two-photon-based analyses and demonstrate cellularity throughout the thickness of the tricuspid chordae tendineae and a dense collagen architecture throughout the thickness. **a** H&E stain of a representative small tricuspid chordae tendineae sample from a posterior belly showing nuclei in dark purple. **b** and **c** Bright-field and (polarized) dark field image of Picrosirius red-stained tricuspid chordae tendineae, respectively

Fig. 4 Tricuspid chordae tendineae mechanics show marginal dependence on leaflet, insertion site, and size. First PK stress-strain for all chordae tendineae split by (a) leaflet, (b) insertion site, (c) tricuspid chordae tendineae size. Data shown are mean \pm 1 standard error. **d** Tangent stiffness computed at 1MPa, again split by leaflet, insertion site, and tricuspid chordae tendineae size. Stiffness was calculated analytically based on the best model fit and is shown as mean \pm 1 standard error. No statistical difference was found for insertion site, leaflet, or size. **e** Correlation analysis between stiffness and tricuspid chordae tendineae (* $p < 0.05$)



those that were non-convex (indicative of tissue damage or clamp slippage) and those with fewer than eight data points (thus leaving us with at least four degrees of freedom when fitting our most complex material model). A complete list of samples is provided in Table 4 in the Appendix. None of those samples were used for two-photon microscopy or histology. For these remaining 53 tests, the average strain rate was $1.20 \pm 0.56\%/s$. Figure 4a shows the average 1st PK stress-strain curves separated by leaflet. We found that tricuspid chordae tendineae, as expected, demonstrated a nonlinear J-shaped behavior. All three curves essentially collapsed on top of each other with little to no difference between leaflets. Additionally, in Fig. 4b, we separated average 1st PK stress-strain curves by insertion site. Here, the stress-strain curves for tricuspid chordae tendineae from

the belly region appear to separate from those of the annular or free edge regions. Similarly, in Fig. 4c, large tricuspid chordae tendineae qualitatively appear to be different from medium and large-sized ones.

Interestingly, at high strains qualitative differences observed in Fig. 4b and c were not supported by our statistical analysis. Neither the calf-modulus, i.e., the slope of the stress-strain curve at 1 MPa, nor the strain at 1 MPa (as a measure for how extensible samples are) significantly differed between leaflet, insertion site, or size, see Fig. 4d. To further analyze stiffness dependence on size without binning tricuspid chordae tendineae size, we performed a correlation analysis between calf stiffness and size, but found only marginal evidence that supports dependence. Specifically, the Pearson correlation coefficient was -0.26

Fig. 5 Representative constitutive model fits for eight models for a “good” data set and a “bad” data set to illustrate the range of data quality. Also shown are the root mean square error (RMSE) for both data sets and each model. Please note, RMSEs vary from those in Table 2, as those are average RMSEs

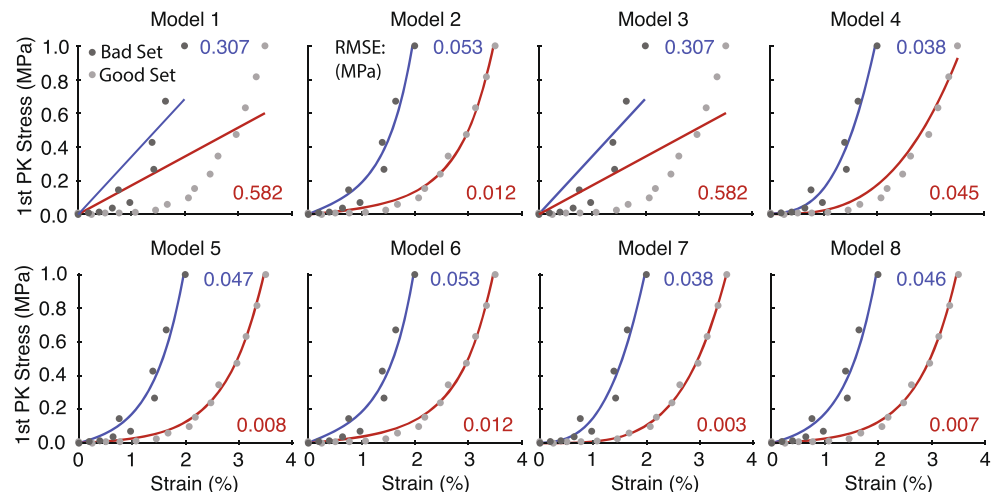


Table 2 Average root mean square error (RMSE) for eight hyperelastic constitutive models listed in Table 1

	Model 1	Model 2	Model 3	Model 4	Model 5	Model 6	Model 7	Model 8
Parameters	1	2	2	2	2	2	3	4
RMSE (MPa)	0.388	0.033	0.388	0.051	0.027	0.032	0.027	0.026

($p=0.0615$), see Fig. 4e. However, we did find significant differences between samples when analyzing the “toe stiffness” of the samples, i.e., the stiffness at small strains. Specifically, we found that the tricuspid chordae tendineae from the anterior leaflet were stiffer than those inserting into the posterior leaflet ($p=0.0221$) and that medium-sized samples were stiffer than large ones ($p=0.0223$). Statistical significance was almost achieved for differences in toe stiffness between tricuspid chordae tendineae inserting into the anterior and the septal leaflet ($p=0.0816$) as well as between small and large tricuspid chordae tendineae ($p=0.0745$). Figure 5 shows two representative mechanical data sets. For this figure, we subjectively selected a “good” data set and a “bad” data set out of our 53 samples to provide transparency for the quality of our data. Fig. 5 also shows the model fit for each of the eight hyperelastic constitutive models, with their respective root mean square errors (RMSE). These fits represent our general findings well in that fits generally increased in quality with an increasing number of parameters.

Table 2 shows the average RMSE across all 53 samples for each model. We found that Model 1 and Model 3 produced the largest RMSE due to their limited ability to reproduce the nonlinear stress-strain behavior of the tricuspid chordae tendineae, as is evident in Fig. 5. The remainder of the models produced remarkably similar fit qualities. Model 8 stood out as producing the closest fit with

an RMSE of 0.026 MPa closely followed by Model 5 and Model 7.

Provided that Model 5 required only two parameters (one less than Model 7 and two less than Model 8), we found Model 5 to be the most appropriate model to represent the mechanics of tricuspid chordae tendineae. In Table 3 we are therefore providing the constitutive parameters of Model 5 fit to the average tricuspid chordae tendineae behavior grouped by leaflet, insertion site, and size.

Discussion

Dysfunction of the tricuspid valve has been associated with significant morbidity and mortality [20]. As the importance of the tricuspid valve to our well-being is increasingly recognized, its mechanics are being studied in more detail. Among recent studies, the in vivo and in vitro mechanics of tricuspid valve leaflets have been characterized in detail [21–25]. Similarly, the dynamics of the tricuspid annulus were studied in humans and in animals [6, 26–28]. In contrast, the tricuspid chordae tendineae have received little attention. Other than the original studies by Lim et al. [11, 12] and recent work by Pokutta-Paskaleva et al. [13], little is known about the constitutive behavior of these tissues and their structure-function relationship. Here, we supplement the current body of knowledge by providing data not

Table 3 Constitutive parameters for Model 5 fit to the average stress-strain data separated by leaflet, insertion site, size, and all included

Model 5	C_1	C_2	RMSE (MPa)
Anterior	0.037	115.773	0.050
Posterior	0.020	126.970	0.034
Septal	0.044	106.660	0.051
Annulus	0.037	102.710	0.077
Belly	0.032	137.606	0.063
Free Edge	0.032	106.959	0.024
Small	0.055	114.393	0.022
Medium	0.046	114.513	0.069
Large	0.017	113.247	0.051
All	0.033	115.451	0.046



only on the mechanics but also on the microstructure of tricuspid chordae tendineae. Additionally, we compare eight constitutive models and their ability to capture the stress-strain behavior of these vital tissues.

To our knowledge, our study is the first full-thickness approach to characterize the microstructure of tricuspid chordae tendineae by quantifying morphological parameters for collagen and cell nuclei. Our microstructural analysis revealed that tricuspid chordae tendineae are highly organized collagenous structures, with a dense cell population throughout that is intimately aligned with its collagen. The presence of cells throughout the tissue thickness likely refutes the notion of chordae tendineae merely being passive “strings”. Dense cellularity implies that tricuspid chordae tendineae, like leaflet tissue, may have the capacity to grow and remodel in response to disease [29]. Especially in light of previous reports that demonstrate an increase in chordal forces under disease conditions, chordal cells are ostensibly involved in chordal adaptation and maladaptation [30]. The collagen and nuclei are highly organized in the longitudinal direction of the tricuspid chordae tendineae shaft, providing its strong longitudinal tensile support. Cell nuclear shape analyses also revealed that near the surfaces of tricuspid chordae tendineae, nuclei are more circular, presumably belonging to endothelial cells. Internal cell nuclei, however, are more elongated and undulated, perhaps due to spatial confinement from the dense collagen. The intimate relationship between collagen orientation, as the tricuspid chordae tendineae’s primary load-bearing constituent, and the cells, could prove to be a direct mechanobiological link between external loads and the internal response mechanisms of the cell. In comparing the tricuspid chordae tendineae of different leaflets and insertion sites, we were unable to distinguish any differences among their collagen and nuclei microstructures. Future studies could perhaps be improved by including an evaluation of elastin microstructure. Similarly, future studies of mitral valve chordae tendineae should perform a similar full-thickness imaging approach of collagen and cell nuclei as we did in the present work.

Our mechanical analysis revealed that our tricuspid chordae tendineae stiffnesses were comparable to previous reports by Pokutta-Paskaleva et al. Specifically, our values (KS) compare to those of Pokutta-Paskaleva et al. (PP) as follows: Anterior, 114 MPa (KS) vs. 114 MPa (PP), Posterior, 123 (KS) vs. 103 MPa (PP), and Septal, 108 (KS) vs. 62 MPa (PP). Also, both we and Pokutta-Paskaleva et al. found that there were insertion-site specific differences in toe stiffness (called “lower tangent modulus” in their work). However, in contrast to Pokutta-Paskaleva, we failed to find

statistically significant differences in the calf stiffness (i.e., stiffness at higher strains) of tricuspid chordae tendineae based on leaflet of insertion [13]. Additionally, they found that septal tricuspid chordae tendineae were more “extensible”, which we also failed to show. On the other hand, we found that there was a dependence between toe stiffness and size, with the largest tricuspid chordae tendineae being the least stiff, which Pokutta-Paskaleva et al. failed to demonstrate. Comparison between our approaches toward identifying the source of discrepancy is difficult: while we tested all leaflets to a 1st PK stress of 1 MPa, Pokutta-Paskaleva et al. tested tricuspid chordae tendineae to failure. Given the nonlinear nature of the chordal constitutive behavior, it is likely that we identified material stiffness at different stresses, which may, at least in part, explain our different findings. Furthermore, it may be interspecies differences that lead to incongruent findings. Future studies comparing tricuspid chordae tendineae from pigs and sheep may shed light on the observed difference.

As to our comparison of eight different constitutive models, we selected these models according to three different criteria. First, we selected only hyperelastic material models. This choice is motivated by being a standard approach toward representing soft collagenous tissues [31]. Of course, this choice omits the time-dependent, viscoelastic behavior seen in these tissues [32] but has been demonstrated to be a useful approach to capturing their most critical behavior. Future approaches may use solid viscoelastic models or biphasic/poroelastic models to capture also the time-dependent behavior of the tricuspid chordae tendineae. Second, we selected models of increasing complexity. The simplest model requires only one parameter, while the most complex model requires four parameters. Third, we selected models that are “Fung-type”, i.e., contain an exponential term, and “non Fung-type”, i.e., don’t contain an exponential term [33]. We found that most models fit the tricuspid chordae tendineae data very well. Exceptions were the Neo-Hookean and Mooney-Rivlin model, both of which failed to capture the highly nonlinear stress-strain behavior of the tricuspid chordae tendineae. On the other hand, all other models fit our data satisfyingly. Not surprisingly, having the most degrees of freedom, the four-parameter Ogden model fit our data best. However, the quality of fits it produced exceeded those of the two-parameter Ogden model only marginally. Thus, we recommend the use of the two-parameter Ogden model to represent the material behavior of the tricuspid chordae tendineae for it is less likely to overfit data. Interestingly, Pokutta-Paskaleva et al. chose this same model; however, the motivations behind this decision are not



clear. Finally, it is noteworthy that non Fung-type models fit data equally well, if not better, than Fung-type models. Fung-type models have been the first choice for modeling soft collageneous tissues for a long time and have only become more dominant with the introduction of the Gasser-Ogden-Holzapfel models [34, 35]. Thus, our findings may also serve as a reminder that other models may fit these data equally well or better.

While our data may be useful to the general reader, it is likely most important to readers that model the tricuspid valve. Specifically, any analytical or numerical model requires knowledge about the material behavior of the model elements. Thus, the quality of any model also depends on the quality of the material data used. Our data and our comparison of material models will be useful to models of the normal tricuspid valve toward understanding its basic mechanics and toward testing medical devices. The most common numerical technique used to model the tricuspid valve is the finite element method. Most commercial and non-commercial finite element codes are distributed with an implementation of the Ogden model, further supporting our choice of this material law [36, 37].

Naturally, our work is subject to limitations. Most importantly, we studied ovine tricuspid chordae tendineae. It is currently unclear to what extent human tricuspid chordae tendineae differ from those of sheep. Thus, when interpreting and extrapolating our data to human subjects, care should be taken. Also, our tissue was not fresh when tested. All tissues were frozen prior to testing. While this is a limitation, we highlight that our tissues were frozen using a solution containing DMSO and proteinase inhibitor, with the intent to limit tissue damage and degradation during freezing and storage. Additionally, we used a controlled-freezing device to ensure an optimal freezing rate. Recently, two papers have also shown that freezing of tricuspid valve tissue has minor effects on its mechanical behavior [38, 39]. From a mechanical perspective, we tracked strain via three fiduciary points and thus limited our strain analysis to two regions. During analysis, we assumed that those strains represent a generally homogeneous strain field within the sample center. While we paid attention to selecting fiduciary points that were “far” from the boundaries, we did not test to what extent the boundary effects from the clamps invalidated our assumption about strain homogeneity. Similarly, our tissues were not perfect cylinders. Specifically, their diameters were not constant along their length and sample cross-sections were unlikely perfect circles. While we tried to address these limitations by measuring diameters at three different locations, we cannot guarantee that they have not affected our results.

Interestingly, Troxler et al. found that in-vitro chordal forces didn't vary as a function of insertion site, but as a function of origin (i.e., from which papillary muscle they emerged) [30]. Future studies should investigate the relationship between tricuspid chordae tendineae origin and their mechanical properties. Also, while many of our proposed models performed similarly well, some models performed better at lower strains, while others performed better at higher strains. Our results are limited in that we only report “global” fits to the entire range of strains. Finally, to the best of our knowledge, the physiological strain rates of tricuspid chordae tendineae are currently unknown. Hence, we have no mean to ensure that our tissues were tested at physiological rates. Future studies should quantify physiological and super-physiological strain rates.

Conclusion

In conclusion, we mechanically tested 53 ovine tricuspid chordae tendineae that we excised from the annular region, the belly, and the free edge of all three leaflets. These tricuspid chordae tendineae did not significantly differ in calf stiffness between different leaflets, insertion sites, or as a function of size. However, we did find marginal differences in toe stiffness between tricuspid chordae tendineae as a function of insertion-site and size. They all showed the classic J-shaped nonlinear stress-strain behavior of collageneous tissues that is due to its highly-organized microstructure which we visualized and quantified via two-photon microscopy and histology. Additionally, we fit eight different hyperelastic constitutive models to our data. Of those models, the two-parameter Ogden model stood out as producing highly accurate results while requiring a small number of parameters. Thus, we recommend this model for future use when modeling the mechanics of tricuspid chordae tendineae. Additionally, we provided the Ogden material parameters for the average stress-strain behavior of our specimen, which can be used in future models of the tricuspid valve.

Acknowledgments This work was supported by the American Heart Association under Award 18CDA34120028 and the National Institutes of Health under Award 1 F31 HL145976-01A1. Dr. Rausch has a speaking agreement with Edwards Lifesciences. No other author has any conflicts to report. We performed all experimental and animal procedures in congruence with the Guide for Care and Use of Laboratory Animals prepared by the National Academy of Science and published by the National Institutes of Health, and the Principles of Laboratory Animal Care, formulated by the National Society for Medical Research. The study protocol was approved by our local Institutional Animal Care and Use Committee (Spectrum Health IACUC No.: 18-01).



Appendix

Table 4 Classification of tricuspid chordae tendineae samples (n=53) by leaflet, insertion site, and size

Subject	Leaflet	Insertion	Size	Subject	Leaflet	Insertion	Size
1	Anterior	Annulus	Large	5	Septal	Annulus	Medium
1	Anterior	Belly	Large	5	Septal	Belly	Medium
1	Anterior	Free Edge	Medium	5	Septal	Free Edge	Medium
1	Posterior	Annulus	Large	5	Anterior	Belly	Medium
1	Posterior	Belly	Medium	5	Anterior	Free Edge	Small
1	Posterior	Free Edge	Large	6	Anterior	Free Edge	Large
1	Septal	Annulus	Medium	6	Septal	Belly	Small
1	Septal	Belly	Medium	6	Septal	Free Edge	Large
1	Anterior	Annulus	Large	6	Septal	Free Edge	Large
2	Anterior	Belly	Medium	6	Anterior	Belly	Medium
2	Anterior	Free Edge	Small	6	Anterior	Free Edge	Large
2	Posterior	Annulus	Small	7	Posterior	Belly	Medium
2	Posterior	Belly	Large	7	Posterior	Free Edge	Large
2	Posterior	Free Edge	Small	7	Septal	Annulus	Medium
2	Septal	Belly	Small	7	Septal	Belly	Medium
2	Septal	Free Edge	Small	7	Septal	Free Edge	Small
2	Anterior	Belly	Large	7	Anterior	Belly	Medium
2	Posterior	Annulus	Small	7	Anterior	Free Edge	Medium
3	Posterior	Free Edge	Small	8	Posterior	Annulus	Medium
3	Anterior	Annulus	Large	8	Posterior	Belly	Small
3	Anterior	Belly	Large	8	Septal	Annulus	Small
4	Posterior	Belly	Large	8	Septal	Belly	Small
4	Septal	Belly	Medium	8	Septal	Free Edge	Medium
4	Anterior	Annulus	Small	8	Anterior	Free Edge	Large
4	Anterior	Belly	Small	8	Septal	Annulus	Large
5	Anterior	Free Edge	Large	9	Septal	Free Edge	Small
5	Posterior	Free Edge	Medium				

References

- Sacks MS, Yoganathan AP (2007) Philos Trans R Soc B: Biol Sciences 362(1484):1369. <https://doi.org/10.1098/rstb.2007.2122>
- Meador WD, Mathur M, Rausch M (2018) Advances in Heart Valve Biomechanics, pp 105–114. https://doi.org/10.1007/978-3-030-01993-8_5
- Cevasco M, Shekar PS (2017) Ann Cardiothoracic Surg 6(3):275
- Mascherbauer J, Maurer G (2010) Eur Heart J 31(23):2841. <https://doi.org/10.1093/eurheartj/ehq303>
- Oliveira DC, Oliveira CG (2019) Cardiol Res 10(4):199. <https://doi.org/10.14740/cr874>
- Lee CH, Laurence D, Ross C, Kramer KE, Babu AR, Johnson EL, Hsu MC, Aggarwal A, Mir A, Burkhart HM, Towner R, Baumwart R, Wu Y, Lee CH, Laurence D, Ross C, Kramer KE, Babu AR, Johnson EL, Hsu MC, Aggarwal A, Mir A, Burkhart HM, Towner R, Baumwart R, Wu Y (2019) Bioengineering 6(2):47. <https://doi.org/10.3390/bioengineering6020047>
- Stevanella M, Votta E, Lemma M, Antona C, Redaelli A (2010) Med Eng Phys 32(10):1213. <https://doi.org/10.1016/j.medengphy.2010.08.013>
- Kong F, Pham T, Martin C, McKay R, Primiano C, Hashim S, Kodali S, Sun W (2018) Ann Biomed Eng 46(8):1112. <https://doi.org/10.1007/s10439-018-2024-8>
- Dabiri Y, Yao J, Sack KL, Kassab GS, Guc-cione JM (2019) Mech Res Commun 97:96. <https://doi.org/10.1016/j.mechrescom.2019.04.009>
- Singh-Gryzbon S, Sadri V, Toma M, Pierce EL, Wei ZA, Yoganathan AP (2019) Annals of Biomedical Engineering. <https://doi.org/10.1007/s10439-019-02243-y>
- Lim KO (1980) Jpn J Physiol 30(3):455. <https://doi.org/10.2170/jjphysiol.30.455>
- Lim KO, Boughner DR, Perkins DG (1983) Jpn Heart J 24(4):539. <https://doi.org/10.1536/ihj.24.539>
- Pokutta-Paskaleva A, Sulejmani F, DelRocini M, Sun W (2019) Acta Biomaterialia 85:241. <https://doi.org/10.1016/j.actbio.2018.12.029>
- Dixon JA, Spinale FG (2009) Circ Heart Fail 2(3):262. <https://doi.org/10.1161/CIRCHEARTFAILURE.108.814459>
- Meador WD, Mathur M, Sugerman GP, Jazwiec T, Malinowski M, Bersi MR, Timek TA, Rausch M (2019) Acta Biomaterialia. <https://doi.org/10.1016/j.actbio.2019.11.039>



16. Meador WD, Sugerman GP, Story HM, Seifert AW, Bersi MR, Tepole AB, Rausch M (2019) *Acta Biomaterialia* (xxxx). <https://doi.org/10.1016/j.actbio.2019.10.020>
17. Rezakhaniha R, Agianniotis A, Schrauwen JTC, Griffa A, Sage D, Bouten CVC, van de Vosse FN, Unser M, Stergiopoulos N (2012) *Biomech Model Mechanobiol* 11(3–4):461
18. Ogden RW, Saccomandi G, Sgura I (2004) *Comput Mech* 34(6):484. <https://doi.org/10.1007/s00466-004-0593-y>
19. Singmann H, Bolker B, Westfall J (2015) *Analysis of Factorial Experiments*, package ‘afex’
20. Enriquez-Sarano M, Messika-Zeitoun D, Topilsky Y, Tribouilloy C, Benfari G, Michelena H (2019) *Progress in cardiovascular diseases*
21. Mathur M, Jazwiec T, Meador WD, Malinowski M, Goehler M, Ferguson J, Timek TA, Rausch M (2019) *Biomech Model Mechanobiol*. <https://doi.org/10.1007/s10237-019-01148-y>
22. Khoiy K, Biswas D, Decker TN, Asgarian KT, Loth F, Amini R (2016) *J Biomech Eng* 138(11):111006. <https://doi.org/10.1115/1.4034621>
23. Pham T, Sulejmani F, Shin E, Wang D, Sun W (2017) *Acta Biomater* 54:345. <https://doi.org/10.1016/j.actbio.2017.03.026>
24. Laurence D, Ross C, Jett S, Johns C, Echols A, Baumwart R, Townner R, Liao J, Bajona P, Wu Y, Lee CH (2019) *J Biomech* 83:16. <https://doi.org/10.1016/j.jbiomech.2018.11.015>
25. Spinner EM, Shannon P, Buice D, Jimenez JH, Veledar E, Del Nido PJ, Adams DH, Yoganathan AP (2011) *Circulation* 124(8):920. <https://doi.org/10.1161/CIRCULATIONAHA.110.003897>
26. Rausch M, Malinowski M, Meador WD, Wilton P, Khaghani A, Timek TA (2018) *Cardiovascul Eng Technol* 9(3):365. <https://doi.org/10.1007/s13239-018-0367-9>
27. Malinowski M, Jazwiec T, Goehler M, Quay M, Bush J, Jovinge S, Rausch M, Timek T (2018) *Journal of Thoracic and Cardiovascular Surgery*. <https://doi.org/10.1016/j.jtcvs.2018.08.110>
28. Rausch M, Mathur M, Meador WD (2019) *GAMM-Mitteilungen*, pp e201900012. <https://doi.org/10.1002/gamm.201900012>
29. Rausch M (2020) *Current opinion in biomedical engineering*
30. Troxler LG, Spinner EM, Yoganathan AP (2012) *J Biomech* 45(6):1084
31. Humphrey JD (2003) *Proc R Soc Math Phys Eng Sci* 459(2029):3. <https://doi.org/10.1098/rspa.2002.1060>
32. Mow VC, Hou JS, Owens JM, Ratcliffe A (1990) *Biomechanics of Diarthrodial Joints*. Springer, New York, pp 215–260. https://doi.org/10.1007/978-1-4612-3448-7_8
33. Fung YC (1967) *Amer J Physiol* 213(6):1532. <https://doi.org/10.1152/ajplegacy.1967.213.6.1532>
34. Holzapfel GA, Gasser TC, Ogden RW (2000) *J Elast* 61(1/3):1
35. Gasser TC, Ogden RW, Holzapfel GA (2006) *J R Soc Interface* 3(6):15. <https://doi.org/10.1098/rsif.2005.0073>
36. Maas SA, Ellis BJ, Ateshian GA, Weiss JA (2012) *J Biomech Eng* 134(1):011005. <https://doi.org/10.1115/1.4005694>
37. Dassault Systemes (SIMULIA) (2014) Providence, RI. Abaqus 6.14 Documentation
38. Duginski GA, Ross C, Laurence D, Johns CH, Lee CH (2020) *J Mech Behav Biomed Mater* 101(July 2019). <https://doi.org/10.1016/j.jmbbm.2019.103438>
39. Salinas SD, Clark MM, Amini R (2019) *Journal of Biomechanics* (xxxx), pp 109462. <https://doi.org/10.1016/j.jbiomech.2019.109462>

Publisher's Note Springer Nature remains neutral with regard to jurisdictional claims in published maps and institutional affiliations.

Affiliations

K. J. Smith¹ · M. Mathur² · W. D. Meador³ · B. Phillips-Garcia⁴ · G. P. Sugerman³ · A. K. Menta³ · T. Jazwiec^{5,6} · M. Malinowski^{5,7} · T. A. Timek⁵ · M. K. Rausch^{1,3,8}

¹ Department of Aerospace Engineering & Engineering Mechanics, University of Texas at Austin, Austin, TX, USA

² Department of Mechanical Engineering, University of Texas at Austin, Austin, TX, USA

³ Department of Biomedical Engineering, University of Texas at Austin, Austin, TX, USA

⁴ Department of Biological Sciences, University of Texas at Austin, Austin, TX, USA

⁵ Division of Cardiothoracic Surgery, Spectrum Health, Grand Rapids, MI, USA

⁶ Department of Cardiac, Vascular and Endovascular Surgery and Transplantology, Medical University of Silesia in Katowice, Silesian Centre for Heart Diseases, Zabrze, Poland

⁷ Department of Cardiac Surgery, Medical University of Silesia School of Medicine in Katowice, Katowice, Poland

⁸ Oden Institute for Computational Engineering and Sciences, University of Texas at Austin, Austin, TX, USA

